Earth's Future

RESEARCH ARTICLE
10.1029/2023EF003698

Special Section:
Quantifying Nature-based Climate Solutions

Impact of Climate on the Global Capacity for Enhanced Rock Weathering on Croplands

Seung H. Baek[1], Yoshiki Kanzaki[2], Juan M. Lora[1], Noah Planavsky[1,3], Christopher T. Reinhard[2], and Shuang Zhang[4]

[1]Department of Earth and Planetary Sciences, Yale University, New Haven, CT, USA, [2]School of Earth and Atmospheric Sciences, Georgia Institute of Technology, Atlanta, GA, USA, [3]Yale Center for Natural Carbon Capture, Yale University, New Haven, CT, USA, [4]Department of Oceanography, Texas A&M University, College Station, TX, USA

Seung H. Baek and Yoshiki Kanzaki contributed equally to this work.

Key Points:

- Enhanced rock weathering (ERW) with fixed annual application rates of 10 tons of basalt dust per hectare on 1,000 global cropland sites sequesters 64 gigatons of CO_2 over 2006–2080
- Extrapolated to *all* croplands, ERW with a fixed application rate of 10 tons of basalt dust per hectare sequesters 215 gigatons of CO_2 over 2006–2080
- ERW is resilient to global climate change but is much more efficient over hot and humid environments

Supporting Information:

Supporting Information may be found in the online version of this article.

Correspondence to:

S. H. Baek,
seunghun.baek@yale.edu

Citation:

Baek, S. H., Kanzaki, Y., Lora, J. M., Planavsky, N., Reinhard, C. T., & Zhang, S. (2023). Impact of climate on the global capacity for enhanced rock weathering on croplands. *Earth's Future*, *11*, e2023EF003698. https://doi.org/10.1029/2023EF003698

Received 3 APR 2023
Accepted 7 JUL 2023

Abstract Enhanced rock weathering (ERW) on croplands has emerged as an economically and ecologically promising negative emissions technology. However, estimated total carbon sequestration potential from ERW on croplands and its potential sensitivity to climate conditions requires further understanding. Here we combine 1-D reactive transport modeling with climate model experiments to simulate ERW on ~1,000 agricultural sites globally. Applying a fixed rate of 10 tons of basalt dust per hectare on these sites sequesters 64 gigatons of CO_2 over a 75-year period; when extrapolated to *all* agricultural land, ERW sequesters 217 gigatons of CO_2 over the same time interval. However, we find that a significant fraction of applied basalt does not weather even on a multidecadal timescale, indicating the need to optimize application strategies for cost effectiveness. We find that ERW becomes modestly more effective with global warming and predict that the payback period for a given ERW deployment is significantly shorter in hot and humid environments currently coinciding with relatively low per-capita incomes. These results provide strong impetus for investment in agricultural reform in developing economies and highlight an additional potential co-benefit of ERW.

Plain Language Summary Enhanced rock weathering (ERW) on croplands is a promising negative emissions concept that accelerates natural weathering by amending soils with crushed rock. Our simulations of ERW with a fixed rate of 10 tons of basalt dust per hectare on all global croplands suggest ERW can sequester >200 gigatons of CO_2 over a 75-year period. This suggests that cost and logistical concerns, rather than weathering potential, are likely to be the key limiting factors for large-scale deployment of enhanced weathering. Notably, ERW is resilient to global climate change and becomes more effective with global warming. ERW is moreover far more efficient in hot and humid environments currently coinciding with relatively low per-capita gross domestic product economies. Our study provides strong support for the assertion that ERW represents a resilient carbon capture strategy that is non-competitive for arable land and can foster CO_2 removal at the gigaton scale.

1. Introduction

Anthropogenic emissions of carbon dioxide (CO_2) and other greenhouse gases over the past ~150 years have contributed to global temperatures increasing by about 1.2°C relative to the preindustrial era (World Meteorological Organization, 2020), with the rate of warming accelerating in recent decades (NOAA, 2021). These trends are concerning given that global warming (a) pushes Earth's climate system toward more frequent and more extreme weather (Baek & Lora, 2021; Baldwin et al., 2019; Cook et al., 2014; Payne et al., 2020; Williams et al., 2020); (b) leads to environmental degradation (including soil, vegetation, and water resource degradation; Allen et al., 2010; Almagro et al., 2017; Burrell et al., 2020; Gonzalez et al., 2010; Lindner et al., 2010; Midgley & Bond, 2015; Zhang et al., 2017); and (c) causes sea levels to rise from thermal expansion of seawater and added meltwater (Mengel et al., 2016; Rahmstorf, 2007). The Intergovernmental Panel on Climate Change (IPCC) has responded by delineating numerous mitigation pathways with the potential to limit global warming to 1.5–2°C above preindustrial levels by 2100 (IPCC, 2018). Importantly, *all* mitigation pathways stipulate the active removal of atmospheric carbon dioxide (in addition to drastic cuts in emissions) on the order of 100 to 1,000 gigatons (billion tons) within the next century to keep total warming below 1.5°C (IPCC, 2018).

Among various negative emissions technologies (Campbell et al., 2022; Fawzy et al., 2020; Jeswani et al., 2022), enhanced rock weathering (ERW) has high potential for rapid scaling since it can leverage existing infrastructure

for its application (Fuss et al., 2014, 2018; Minx et al., 2018). ERW is based on the natural process of chemical weathering, which sequesters atmospheric carbon dioxide through dissolution of silicates or carbonates (via carbonic acid). Natural weathering stores carbon in the oceans as bicarbonate ions for millennia, and even longer when mineral carbonates (produced by calcifying organisms) are buried in marine sediments (e.g., Archer et al., 1997; Ridgwell & Hargreaves, 2007). This process currently removes about ∼1.0 gigatons of atmospheric carbon dioxide per year (IPCC, 2022; Strefler et al., 2018). Although silicate weathering will ultimately balance anthropogenic CO_2 release rates over geological time scales, the natural response time of this process is orders of magnitude too slow to mitigate anthropogenic fossil fuel emissions (Archer et al., 1997). The goal of ERW is to accelerate natural weathering by (a) amending soils with crushed rocks (particularly silicates) and (b) concentrating weathering activity on regions where rock/mineral dissolution is favored (e.g., Beerling et al., 2020; Goll et al., 2021; Taylor et al., 2016).

ERW could in theory be applied to any vegetated area (e.g., Goll et al., 2021). However, logistical accessibility for transport of silicate feedstock significantly improves economic viability. In this respect, ERW on croplands (which are road accessible, in contrast to most forested lands) has emerged as a promising, scalable approach toward CO_2 removal (e.g., Beerling et al., 2020), with ecological co-benefits, such as (a) rejuvenation of depleted soils, (b) improved crop yields (from additional nutrient supply from rock feedstock), and (c) mitigation of ocean acidification (from addition of alkalinity), that make ERW socially desirable (Beerling et al., 2018; Strefler et al., 2018; Taylor et al., 2016). Estimates of carbon capture from ERW on global croplands nevertheless remain sparse, with only one existing study to our knowledge (Beerling et al., 2020). Moreover, the sensitivity of such estimates to regional climate and global climate change has not yet been investigated. Therefore, there is an obvious need for additional model-based and empirical constraints on the potential for ERW to act as a means of large-scale CO_2 removal.

Here, we provide model-based, first-order estimates of the global CO_2 removal potential of ERW on cropland systems. We use a newly developed 1-dimensional reactive transport model (Soil Cycles of Elements simulator for Predicting TERrestrial regulation of greenhouse gases; SCEPTER) to simulate ERW (Kanzaki et al., 2022). This soil biogeochemical model represents an advancement in the complexity of models used to predict enhanced weathering behavior on a global scale. In particular, the model includes comprehensive particle size distribution and specific surface area tracking, regionally specific host soil development, and a transient soil spin-up (see Supporting Information S1 for more details). We combine SCEPTER with global climate model simulations with the dual aims of (a) estimating the total CO_2 sequestration potential of ERW on global croplands and (b) characterizing the sensitivity of this potential to regional climate conditions. Collectively, our efforts provide an illustrative example of the extent to which ERW on Earth's croplands could mitigate global warming in the coming decades. Our modeling framework furthermore provides strong independent support for previous work suggesting that widespread deployment of enhanced weathering on cropland systems has the potential to drive gigaton-scale CO_2 removal annually (Beerling et al., 2020). However, our results also highlight the potential for low weathering efficiency during ERW deployment with coarse-grained feedstock, with significant material remaining undissolved on decadal timescales.

2. Data and Methods

2.1. Identifying 70%+ Cropland Grid Points

We identify cropland sites using a global 1-km consensus land-cover product integrating four remote sensing-derived base products (see Tuanmu & Jetz, 2014 for details). This consensus product provides information on the prevalence of 12 different land-cover classes for every nominal 1-km pixel on the globe (except Antarctica), from which we define cropland to be the cultivated and managed vegetation land-cover classes. We degrade the cropland prevalence from 1-km pixel resolution to 1° grid resolution via averaging, then select grid points where cropland proportion is at least 70% of the land cover in each grid point. This process yields 963 grid points representing global cropland. We estimate the land area of cropland in each 1° grid point by multiplying the percent cropland of each grid point with the grid area, using a 1° latitude = 110.6 km and 1° longitude = 111.3 * cos(latitude) conversion. Our reactive transport model is then applied to these 963 grid points, from which we derive a global ERW estimate.

2.2. 1-Dimensional Reactive Transport Modeling

SCEPTER is a 1-D reactive transport model that simulates weathering, with options to: (a) enable variable soil mixing regimes (such as natural bioturbation or tilling operated at croplands); (b) track size distributions of soil

mineral particles and calculate their surface areas; (c) trace targeted minerals and/or soil organic matter to the soil surface; and (d) allow temporal changes in climatological boundary conditions (such as surface temperature, water infiltration rate and soil water content). Some of our model features (e.g., d above) have already been implemented by previous ERW modeling approaches (cf. Beerling et al., 2020; Kantzas et al., 2022), but others are new, including mechanistic soil mixing, explicit tracking of soil organic matter and soil CO_2 in depth and time, and basalt application in two steps, that is, basalt application experiments branching off from spin-ups that only implement natural weathering without any basalt application (see below for more details, and Kanzaki et al. (2022) for a full description of SCEPTER). We note that while the shrinking-core model in SCEPTER has reproduced dissolution/precipitation of minerals observed in the laboratory, it has not yet been tested against ground basalt applied in the field. In addition, the simulations presented here do not account for passivation effects. Although this should render our conclusion that dissolution efficiency can be low with coarse-grained feedstocks conservative, it may lead to an overestimation of overall capture potential at a given feedstock application rate.

We use SCEPTER on the 963 identified cropland sites around the globe, using each site's unique set of lithological/geomorphological and climate parameters as inputs. We derive lithology data from Hartmann and Moosdorf (2012), soil organic matter data from Hengl et al. (2017), and erosion rate data from Larsen et al. (2014). We derive detailed soil respiration data based on the mass balance of organic matter in soil (using global datasets of soil organic matter weight fractions and erosion rate). The calculation assumes mass balance of soil organic matter within 30 cm between erosion and respiration, the latter of which is formulated with organic matter decay reflecting its temperature dependence (3 of Q_{10}, a factor of increase in the rate by each 10°C temperature increase; Wang et al., 2010), along with the soil porosity (0.5) and particle densities of soil minerals (~2.6 g cm^{-3}) and organic matter (1.5 g cm^{-3}) in accord with assumed boundary conditions for SCEPTER (see Kanzaki et al., 2022). Specifically, organic matter rain (g m^{-2} $year^{-1}$) is specified in SCEPTER as f_{SOM} * (2.6e6 * (1. − f_{SOM}) + 1.5e6 * f_{SOM}) * (1.− 0.5) * (w + k_{SOM} * 0.3 * 0.5), where f_{SOM} is the weight fraction of soil organic matter, w is erosion rate (m $year^{-1}$), and k_{SOM} is a decay constant ($year^{-1}$), given by $k_{SOM,ref}$ * 3^(tc − tc_{ref})/10 where $k_{SOM,ref}$ and tc_{ref} are reference decay constant (1/8 y^{-1}; Chen et al., 2010) and temperature (15°C).

We input local climate parameters relevant for weathering—surface temperature, total liquid runoff, and volumetric soil moisture at 21 cm depth—from the Community Earth System Model version 1 (CESM1), a fully coupled global climate model, at grid points corresponding to the 1° grid of the 963 cropland pixels with all relevant CESM1 outputs re-gridded to the common 1° grid resolution using bi-linear interpolation. SCEPTER experiments that do not apply basalt dust are conducted under natural bioturbation mixing conditions; SCEPTER experiments with basalt dust application are conducted with tilling for cropland grid cells. We note that the grid resolution in CESM1 is potentially coarse compared to expected variability in weathering rates on the field scale. Although we consider our approach appropriate for the goal of providing first-order estimates of weathering rate and efficiency across broad regions of arable land, performing more high-resolution regional (or field-scale) analysis for targeted deployments will be an important avenue for future work.

Prior to any ERW simulations, we initialize SCEPTER by running a 100 Kyr spin-up experiment with local, observed soil parameters and 850–1850 CE millennium averages of surface temperature, total liquid runoff, and volumetric soil moisture at 21 cm depth (note that the climate variables thus have no seasonal cycle); we do this without any basalt dust application and under natural bioturbation mixing conditions. This 100 Kyr initialization is done so that soil mineralogy can evolve from imposed parent-rock lithology and achieve steady state. The millennium averages of the climate variables are calculated from one member (Ensemble Member #2) of the "Last Millennium Ensemble" Project, which forces the CESM1 model with reconstructed estimates of natural and pre-industrial radiative forcing (see Otto-Bliesner et al., 2016 for details). Outputs from the Last Millennium Ensemble are available on ~1.9° latitude by 2.5° longitude grid resolution.

We follow up these 100 Kyr initializations with seasonal calibrations that run SCEPTER for an additional 86 years representing the 1920–2005 historical interval, again under natural bioturbation mixing conditions and without any basalt dust added. We use monthly climate variables (surface temperature, total liquid runoff, volumetric soil moisture at 21 cm depth) simulated by a 20-member ensemble mean of the CESM1 Large Ensemble (members #2–21; Kay et al., 2015) forced with historical radiative forcing over 1920–2005. In using monthly climate variables, the calibration experiments impose seasonality, which was absent in the 100 Kyr initialization. Specifically, we use the 20-member ensemble mean, which drastically reduces the influence of internal climate variability

and thus represents the radiatively forced response of 1920–2005. For some of the 963 sites, we replace negative total liquid runoff values (which are inherent in the climate model output) with very small positive values (10^{-15} mm/s) so that runoff is always positive even with seasonal fluctuations. Climate outputs from the Large Ensemble are available on ~1° grid resolution.

After initialization and seasonal calibration, we apply 10 tons of basalt dust per hectare on the 963 cropland sites every year for 75 years representing the 2006–2080 interval. This basalt application rate is designed to yield a conservative estimate for global carbon dioxide removal (CDR) potential, as it is on the lower end of application rates assumed in previous work (Beerling et al., 2020; Goll et al., 2021) but is broadly consistent with conventional rates of ag-lime application (Galinato et al., 2011; Lukin & Epplin, 2003; T. O. West & McBride, 2005). As before, we use local, site-specific observed soil parameters but use monthly climate variables simulated by the CESM1 Large Ensemble (20-members; members #2–21), this time under the Representative Concentration Pathways 4.5 and 8.5 W/m^2 (RCP4.5 and RCP8.5) scenarios. The two future scenario basalt application experiments are thus branched out of the historical simulations without basalt application. CDR is then estimated based on differences in cumulative carbon fluxes in the basalt application experiments relative to the end of the historical experiment. Again, for some of the sites we replace negative runoff values with very small positive values (10^{-15} mm/s) so that runoff is always positive even with seasonal fluctuations. ERW experiments with basalt application are conducted under tilling conditions operated at croplands. While appropriate for our purposes, we note that the use of monthly climate variables (as opposed to, for instance, daily variables) may not fully capture natural wet-dry/cool-hot cycles or percolation events. This may in turn lead to under- or overestimated mineral dissolution rates and represents an obvious target for future research (Buckingham et al., 2022; Calabrese et al., 2022; L. J. West et al., 2023).

The above-described procedures successfully simulate ERW on 929 (927) out of the 963 sites (>96% success rate) under the RCP8.5 (RCP4.5) scenario; SCEPTER did not converge for the other 34 (36) sites (representing <4% of locations), mostly due to (a) climate boundary conditions that make convergence untenable during the 100 Kyr spin-up experiment (e.g., zero/NaN values for runoff [mm/s], soil moisture [unitless fraction], or temperature [K]) and/or (b) high assumed organic matter flux (e.g., >3,000 g C/m^2 year).

Spin-up experiments (which do not have basalt application) and basalt application simulations described above are conducted in the same way as the "pulsed basalt application" example in Kanzaki et al. (2022), with full tracking of particle size distributions of individual minerals; however, tilling is represented by an inversion mixing in this paper (see Equation S1 in Supporting Information S1), rather than as homogeneous mixing. We also track the evolution of solid, aqueous, and gaseous species. Tracked solid species include: albite, anorthite, K-feldspar, forsterite, fayalite, diopside, phlogopite, tremolite, hedenbergite, quartz, goethite, kaolinite, Ca-beidellite, Mg-beidellite, gypsum, calcite, aragonite, dolomite, and one class of soil organic matter; tracked aqueous species include: Ca, Mg, Na, K, Si, Al, Fe(II), Fe(III), and SO_4; tracked gaseous species include: O_2 and CO_2; Fe(II) oxidation to Fe(III) by O_2 is also explicitly simulated as an extra reaction in addition to dissolution/precipitation of the above-listed solid species. Fundamental thermodynamic (e.g., particle density, molar volume/weight, chemical formula, and solubility of solid species; thermodynamic constants for formation of dependent aqueous species) and kinetic (e.g., rate constants of dissolution/precipitation for solid species and extra reactions; molecular diffusion coefficients for aqueous/gaseous species) data are given in Kanzaki et al. (2022).

For gas and aqueous species, upper boundary conditions are given by fixed concentration values equivalent to the chemical composition of the atmosphere (0.21 and $10^{-3.5}$ atm for O_2 and CO_2, respectively) and rainwater (assumed here as pure water for simplicity), respectively; the lower boundary is assumed to be impermeable for diffusive flux. Soils are assumed to have the solid phase composition of an unaltered rock at depth: the lower boundary conditions for solid species are given as fixed concentrations, which are obtained from lithology data. The simulated soil column is 50 cm and divided into 30 layers, and the initial porosity for spin-up is assumed to be 0.5 regardless of location. Although a coarser discretization of the soil column may suffice, finer discretization is still desirable given that basalt may accumulate on topsoil when mixing is inefficient. Organic matter is applied continuously at the surface at a rate described above and mixed to a 25 cm depth via natural bioturbation (Fickian mixing: see Kanzaki et al. (2022) for detailed formulation) along with other solid species (listed above), whether basalt is additionally applied or not. When applied, basalt is assumed to have the same mineralogical composition as those adopted by Beerling et al. (2020) and Kanzaki et al. (2022) (Table S1 in Supporting Information S1), with 0.37 g CO_2 as the maximum capture capacity per 1 g basalt. For our "fine-grained" basalt feedstock, initial

particle size distributions are defined as a function of particle radius, equivalent to the sum of 4 log-normal distributions centered at 1, 2, 5, and 20 μm, all with 0.2 log unit standard deviations ($f_{basl}(r) \propto \sum_{i=1}^{4} \exp(-(\log r - \log r_i)^2/0.4)$, where $f_{basl}(r)$ is the initial number of particles as a function of particle radius r in meters and $r_i = 1 \times 10^{-6}$, 2×10^{-6}, 5×10^{-6}, and 20×10^{-6} for $i = 1, \ldots, 4$). The surface roughness is accounted for by using a radius function from Navarre-Sitchler and Brantley (2007) that is also adopted in Beerling et al. (2020) and Kanzaki et al. (2022). Resulting initial surface areas are, for example, 6.6 and 6.5 m^2/g for anorthite and fayalite, respectively, of the basalt. The p80 value of our fine-grained basalt feedstock (the diameter for which 80% of the total basalt mass is made up from particles with a smaller diameter) is calculated to be 100 μm (Figure S3 in Supporting Information S1). Parameter values for our "coarse-grained" basalt are defined by the sum of 2 log normal distributions centered at 0.5 and 5 μm all with 0.5 log unit standard deviations, resulting in a p80 of 1,220 μm and, for example, 0.18 and 0.12 m^2/g surface areas for anorthite and forsterite, respectively. When applied, the basalt is added at the surface and mixed to 25 cm depth by tilling only during the first 0.1 fraction of each year. During the rest of the year soil is left to be mixed to the same depth by natural Fickian bioturbation together with other solid species. Temperature, soil moisture and net water flux are assumed to be depth-independent and are fixed for long-term spin-up but are varied monthly for historical runs and basalt application experiments where the above climate factors are forced by outputs from CESM1.

2.3. Carbon Capture Estimates

The addition of basalt to croplands increases the capacity of land to act as a net CO_2 sink through two primary pathways: (a) the conversion of atmospheric CO_2 to dissolved CO_2 species (mostly HCO_3^-) and the subsequent loss of dissolved CO_2 to rivers and oceans via water flux; and (b) the precipitation of carbonates (mostly calcite; $CaCO_3$) in soil. Beerling et al. (2020) calculated net CO_2 capture as 0.86 times the advective flux change of dissolved CO_2 species plus carbonate precipitation within soil, where the factor of 0.86 accounts for the return of CO_2 to the atmosphere after dissolved CO_2 species arrive at the oceans. For simplicity, we follow this principle and define CO_2 capture as net change in the CO_2 diffusive supply, subtracting out changes in CO_2 supply from soil respiration (that are not caused by basalt addition) and atmospheric CO_2 returned from the ocean (0.14 times the advective flux change of dissolved CO_2 species). That is, total CO_2 capture is equivalent to the change in diffusive CO_2 supply minus the change in CO_2 supply from soil respiration plus 0.14 times the change in advective flux of dissolved CO_2 species. However, we note that this is done primarily for comparative purposes, and that the amount of downstream carbon leakage in river/stream systems and from the coastal ocean subsequent to a given amount of initial CDR through ERW may vary from this (Kanzaki et al., 2023).

2.4. Extrapolation to Grid Points Below the 70% Cropland Threshold

The agricultural land area identified with 70%+ cropland grid points represents only a fraction of total global agricultural land area. In order to scale our results for 70%+ cropland area to overall global cropland we use a nearest neighbor interpolation method in which the total carbon capture estimate of the nearest 70%+ cropland grid point is used to fill in cells below the 70% cropland threshold. We then weight these values by the percent cropland of each cell to derive a total cropland ERW estimate.

3. Results

We identify cropland sites (defined as where cropland proportion is at least 70% of land cover; see Methods) in every continent except Antarctica, with high density of cropland over the American Midwest and southern regions of Canada's Prairie Provinces (North America); Argentina and Brazil (South America); Western Africa and Ethiopia (Africa); eastern Europe and Russia (Europe); India, Thailand, and eastern China (Asia); and southwestern Australia, Victoria, and southern New South Wales (Australia). These cropland sites total 929 grid points, which collectively equal 7,407,423 km^2 of cropland. Total cropland area across all cells is equivalent to 24,694,492 km^2.

Using SCEPTER, we apply a fixed rate of 10 tons of basalt per hectare annually under two RCP scenarios (Figure 1) and explore two grain size distributions (here referred to as "fine," for which the grain size at which 80% of the material passes sieving (p80) is 100 μm, and "coarse," for which p80 = 1,220 μm). This application rate is within the bounds of current limestone soil amendments in many regions (Galinato et al., 2011; Lukin & Epplin, 2003; T. O. West & McBride, 2005) and the relative grain sizes are comparable to waste fines from

10.1029/2023EF003698

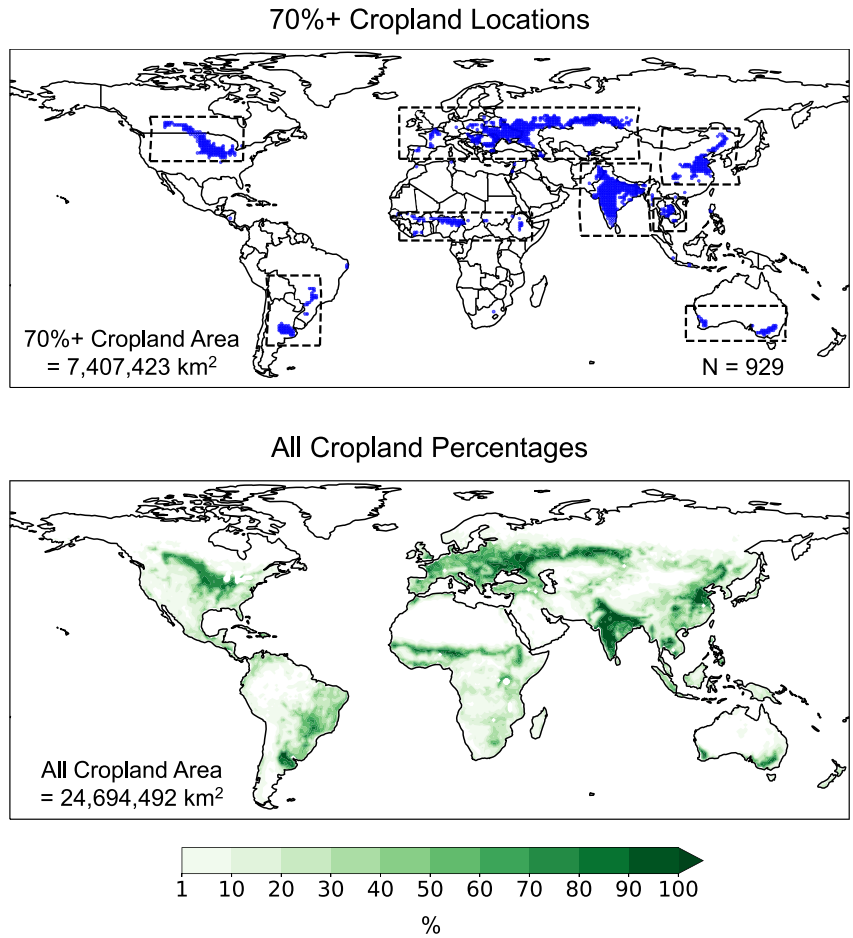

Figure 1. (*Top*) The location of cropland sites across the globe where SCEPTER was successfully applied ($n = 929$). The total cropland area accounted for by these grid points is provided on the lower left corner (weighted by the percentage of agricultural land). (*Bottom*) Percentages of croplands across the globe (including both above and below the 70% agricultural threshold). The total cropland area is provided on the lower left corner (weighted by the percentage of agricultural land).

aggregate production (Adilson et al., 2016; Bullock et al., 2021). Figure 2 shows the total amount of CO_2 captured under both the RCP4.5 and RCP8.5 scenarios, with total CO_2 captured defined as the net change in CO_2 diffusive supply accounting for (a) CO_2 from soil respiration independent of basalt added and (b) an assumed advective CO_2 returned to the atmosphere from the ocean (Figure S1 in Supporting Information S1; see Methods). ERW simulations under both global warming scenarios show considerable heterogeneity in the rate of CO_2 captured, with regional carbon uptake differences far outweighing differences across the RCP4.5 and RCP8.5 scenarios. Most cropland regions over North America (concentrated around the "corn belt" in the American Midwest), South America, and Europe/Russia, for instance, show carbon capture rates of ~1 ton of CO_2 per hectare per year ($tCO_2\ ha^{-1}\ year^{-1}$) in both global warming scenarios, while carbon capture rates over Australia are less than ~0.6 $tCO_2\ ha^{-1}\ year^{-1}$. Cropland grid points over Africa, Thailand, eastern China, and India show higher carbon capture rates of ~1.2–1.6 $tCO_2\ ha^{-1}\ year^{-1}$.

Despite relatively minor impacts from climate change, ERW on croplands depends strongly on regional climatic conditions. Croplands in tropical latitudes and India, for instance, are hotspots of carbon capture over the 2006–2080 interval (Figure 3), likely because they receive significant amounts of solar radiation due to their proximity to the equator and ample precipitation from the Intertropical Convergence Zone and the Indian Monsoon, respectively. Notably, there is significant spatial correlation between total carbon capture estimates for the simulated sites (as shown in Figure 2) and climatological surface temperature over the 2006–2080 interval under the RCP8.5 scenario ($r = 0.51$, $p < 0.01$) ($r = 0.48$, $p < 0.01$ for RCP4.5). Similarly, there is robust spatial correlation between total carbon capture estimates and climatological total liquid runoff ($r = 0.57$, $p < 0.01$) (same for

10.1029/2023EF003698

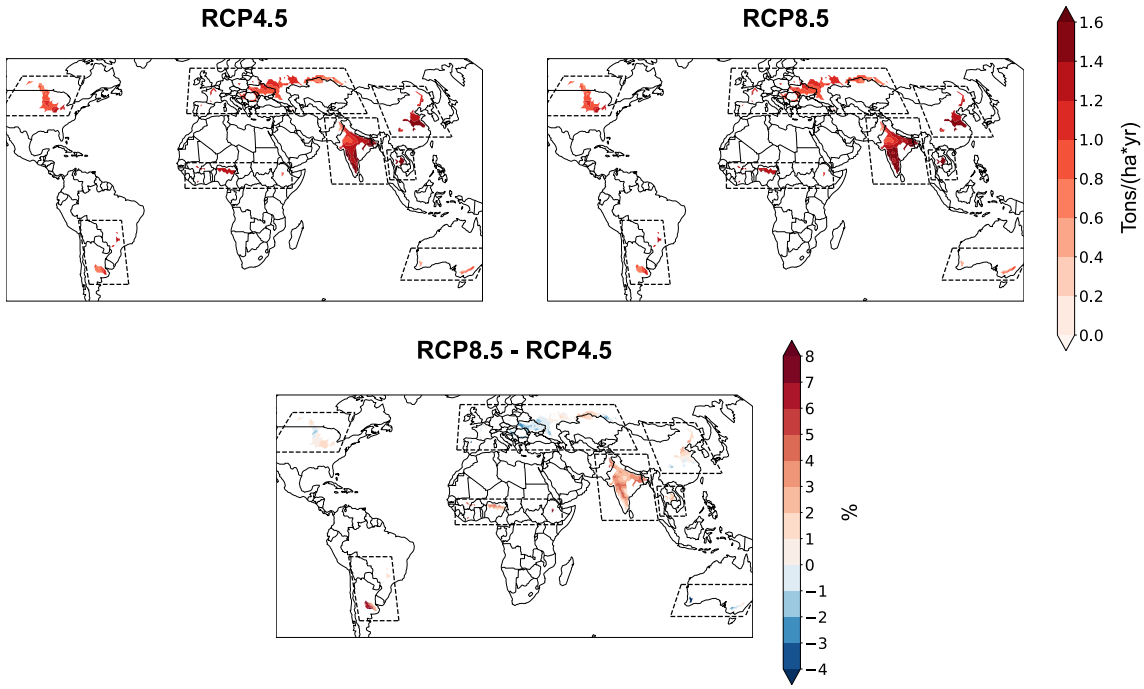

Figure 2. (*Top*) Total enhanced rock weathering (ERW) under the (*left*) RCP4.5 and (*right*) RCP8.5 scenarios. Simulations are performed with a spatially uniform basalt application rate of 10 tons per hectare annually with a uniform fine basalt grain size (p80 = 100 μm). (*Bottom*) Additional total ERW under the RCP8.5 scenario relative to the RCP4.5 scenario, expressed as a percent increase.

RCP4.5). Climatological soil moisture values do not correlate as strongly in space with carbon capture fluxes over the 2006–2080 interval ($r = 0.25$, $p < 0.01$) (same for RCP4.5). Our results are nevertheless consistent with expectations that hot and wet environments will favor rock/mineral dissolution (e.g., Beerling et al., 2020; Goll et al., 2021; Taylor et al., 2016).

We next calculate the total amount of CO_2 captured over the 2006–2080 interval over the simulated cropland cells by region (see Figure 2 for demarcations), weighting the rate of CO_2 capture by cropland percentage (Table 1;

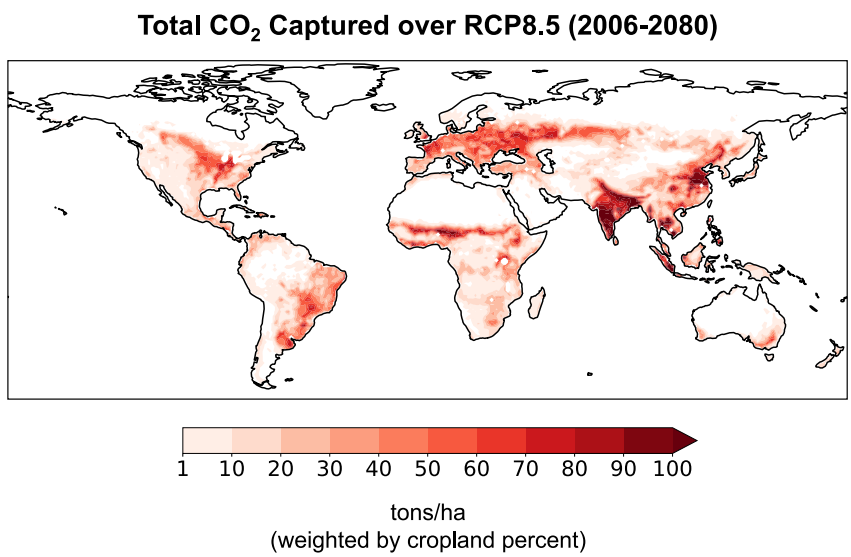

Figure 3. Total CO_2 captured over the 2006–2080 interval under the RCP8.5 scenario. Simulations are performed with a spatially uniform basalt application rate of 10 tons per hectare annually with a fine (p80 = 100 μm) uniform basalt grain size. Carbon capture rates for grid points where cropland is 70% or less of total land area are estimated using the rate of the nearest 70%+ cropland. Total carbon captured over each grid point is weighted by the cropland percentage of that grid point.

Earth's Future

10.1029/2023EF003698

Table 1

(Top) Total Amount of CO_2 Captured Across 70%+ Croplands by Country/Continent (See Figure 2 for Demarcation of Regions) Over the 2006–2080 Interval Assuming Fine Basalt Grain Size (p80 = 100 μm) and a Spatially Uniform Annual Basalt Application Rate of 10 Tons per Hectare Under the (Left) RCP4.5 and (Right) RCP8.5 Scenarios

70%+ croplands only	RCP4.5 total over 2006–2080 (Gton)	RCP8.5 total over 2006–2080 (Gton)
N. America	5.77	5.81
Europe/Russia	15.77	15.73
S. America	2.99	3.07
Africa	5.29	5.59
Australia	1.25	1.23
India	20.15	20.75
Thailand	2.36	2.39
China	8.12	8.18
Other	1.72	1.77
Total	63.4	64.51

All croplands	RCP4.5 total over 2006–2080 (Gton)	RCP8.5 total over 2006–2080 (Gton)
N. America	23.35	23.26
Europe	36.89	36.73
S. America	29.02	28.93
Africa	39.6	40.63
Oceania	3.95	3.92
Asia	81.52	82.85
Global	214.81	216.79

Note. (*Bottom*) Same as (top) but for CO_2 captured across *all* croplands (estimated using nearest neighbor carbon capture rates of grid points meeting the 70% cropland threshold) by continent over the 2006–2080 interval.

10.1029/2023EF003698

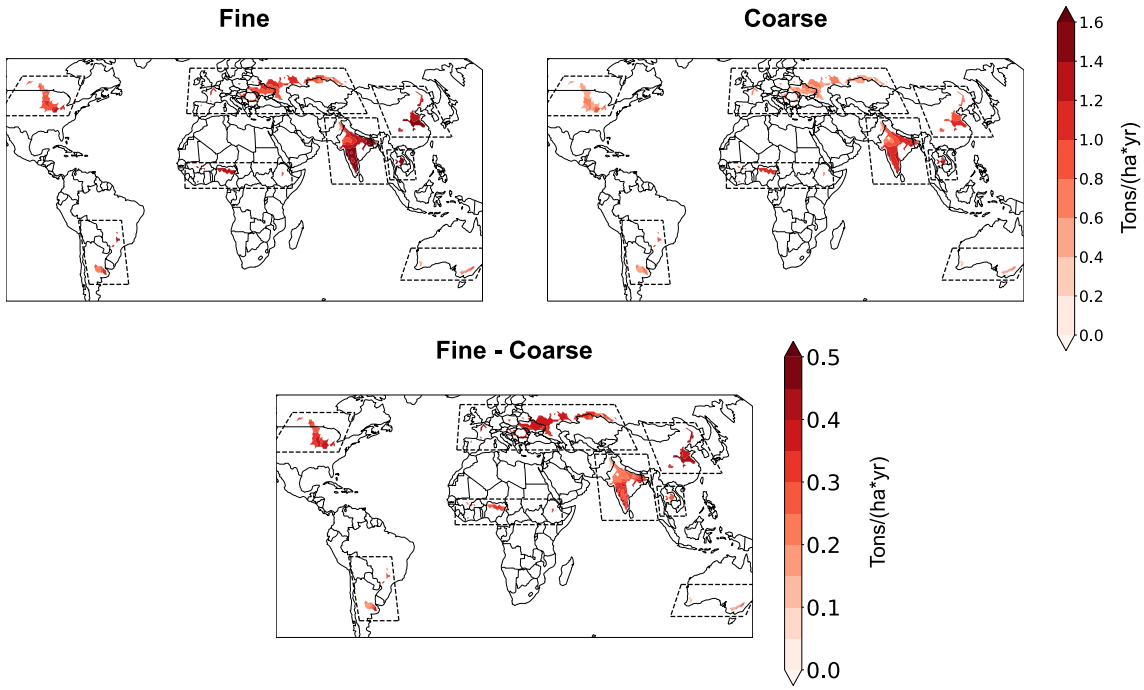

Figure 4. (*Top*) Total enhanced rock weathering (ERW) under the RCP8.5 scenario for (*left*) fine uniform basalt grain size (p80 = 100 μm) and (*right*) coarse uniform basalt grain size (p80 = 1,220 μm). All simulations are performed with a spatially uniform basalt application rate of 10 tons per hectare annually. (*bottom*) Difference in total ERW across the two experiments.

note Figure 2 shows rates without cropland weighting). ERW on the 70%+ cropland cells can capture 63.4 and 64.5 gigatons of CO_2 ($GtCO_2$) under RCP4.5 and RCP8.5 scenarios, respectively, which translates to a global average area-normalized CDR rate of 1.14 tCO_2 ha^{-1} $year^{-1}$ and 1.16 tCO_2 ha^{-1} $year^{-1}$. Consistent with the above results, this analysis highlights the importance of regional heterogeneity in ERW potential. In our simulations, India alone, with its large cropland area and high ERW rates, accounts for 32% of total carbon captured globally. Despite lower ERW rates, Europe/Russia have a disproportionate amount of cropland area and thus account for another 24%–25%. Lastly, Africa accounts for 8%–9% of total carbon captured despite only accounting for a minor portion of total global cropland area due to very high ERW rates.

Agricultural land area identified with our 70%+ cropland threshold represents only a fraction of the total global agricultural land area. We therefore attempt to provide a first-order estimate for global carbon capture across *all* agricultural lands globally using nearest neighbor interpolation (Table 1; Figure 3). Globally, we estimate ERW on croplands can capture as much as ~215 $GtCO_2$ over the 2006–2080 interval (Table 1), with substantial regional heterogeneity in capture potential. Africa and Asia alone, for instance, demonstrate ERW carbon capture potentials of up to 40.6 and 82.9 $GtCO_2$, respectively, over the simulation period. Oceania in contrast shows minimal ERW potential (a total of ~4 $GtCO_2$). We note that this global potential of ~215 $GtCO_2$ sequestered over the 2006–2080 interval is well above the lower end of the range stipulated by IPCC mitigation pathways to limit global warming to 1.5°C (i.e., 100–1,000 gigatons by 2100). Though a rough approximation, our estimates thus support the notion that ERW on global croplands has the potential to play an integral role in any comprehensive negative emissions strategy, especially when considering that feedstock processing and application rates have not been optimized in our simulations.

Finally, we characterize the sensitivity of ERW to basalt grain size. To do this, we use SCEPTER and apply a fixed rate of 10 tons of coarse-grained basalt sand (p80 = 1,220 μm) per hectare annually (Figure 4). As with fine-grained basalt application, additional global warming from the RCP8.5 scenario relative to RCP4.5 scenario has only a modest influence on ERW with coarse-grained basalt application: global carbon capture rates with coarse-grained basalt application are 0.81 tCO_2 ha^{-1} $year^{-1}$ and 0.83 tCO_2 ha^{-1} $year^{-1}$, under the RCP4.5 and RCP8.5 scenarios, respectively. However, overall carbon capture is, on average, ~70% of that achieved in our "fine-grained" simulation even after decades of weathering.

4. Discussion

Using SCEPTER and a series of climate model experiments, we have simulated ERW by applying 10 tons of fine-grained basalt sand and silt per hectare per year on 963 agricultural sites across the globe. These 963 sites alone can sequester ~64 $GtCO_2$ over the 2006–2080 interval. From these results, we extrapolate to first-order that ERW can sequester ~215 $GtCO_2$ over the same interval when applied to all cropland locations worldwide. Collectively, our results provide strong support for the notion that ERW on global croplands can foster CO_2 removal at gigaton scale.

Although there are large regional differences in weathering rates linked to local climates, future global warming has a minor effect on global average CDR rates (~2% increase with a high emissions scenario). This contrasts with soil organic carbon storage, which becomes significantly less stable under higher temperatures and may become a carbon source with continued global warming (Crowther et al., 2016; Davidson & Janssens, 2006; Nottingham et al., 2019; Zhao et al., 2021). Despite small influences from climate change, ERW is nevertheless sensitive to regional climate variability. Notably, ERW is more efficient—for example, more basalt is weathered over a given time interval—in hot and wet environments concentrated around the tropics currently coinciding with economically developing regions (Figures 2 and 4). Ramp-up speed for ERW after initial basalt application is in general faster in regions of relatively low per-capita income (Figure S2 in Supporting Information S1), with shorter time to reach full-capacity sequestration rates. This supports the notion that there is strong potential for ERW in developing economies, even though precision agriculture is uncommon and the infrastructure needed for large-scale basalt deployment is not currently in place. Therefore, our results provide strong impetus for investment in agricultural reform in developing economies, which would represent an additional co-benefit of ERW for regional stakeholders.

Finally, we find that basalt grain size is an important parameter for CDR effectiveness and unit cost of CDR deployment ($/ton of CO_2 captured), with coarser grained basalt feedstock achieving substantially less cumulative CDR than fine-grained basalt feedstock. With coarser grained basalt, large portions of the applied basalt are likely to remain unweathered even after decades within a soil. The potential for persistence of significant amounts of basalt feedstock in a soil column highlights one potential problem with pursuit of ex ante carbon credit schemes prior to extensive data-model comparison. Similarly, these results highlight the pressing need for feedstock grain sizes and application rates to be optimized for local conditions in order to promote both greater CO_2 capture efficiency and more favorable techno-economics in the global North than the global South. Although our estimate of the theoretical potential of enhanced weathering in croplands is very likely conservative, our work nevertheless provides additional support (see Beerling et al., 2020) for the assertion that ERW represents a scalable, resilient carbon capture strategy that is non-competitive for arable land. Overall, this bolsters the case that there is tremendous potential, from a geochemical point of view, for enhanced weathering to foster carbon dioxide removal at scale. Therefore, the geochemical weathering potential (which is at the gigaton-scale) and hard infrastructure (e.g., farm equipment needed for soil amendments) are less likely to limit the scaling of ERW than gaps in the structure of carbon marketplaces and the nascent state of standards for monitoring, reporting, and verification.

Data Availability Statement

All CESM1 model data are publicly available through the Casper cluster (/glade/campaign/cesm/collections/cesmLME/CESM-CAM5-LME/) or through the Climate Data Gateway (https://www.cesm.ucar.edu/community-projects/lme/data-sets). The version of the SCEPTER code used in this study is available at (Kanzaki, 2022).

Acknowledgments
This work was supported by the Department of Earth and Planetary Sciences of Yale University. SHB, JML, and NP would like to acknowledge support from the Yale Center for Research Computing (YCRC). YK and CTR would like to acknowledge support from the Partnership for an Advanced Computing Environment (PACE) at the Georgia Institute of Technology. SZ would like to thank the support from the Yale Center for Research Computing.

References

Adilson, C. D., Claudete, G. R., Marcos, L. S. O., Elba, C. T., Rubens, M. K., Silvio, R. T., et al. (2016). Chemical characterization, nano-particle mineralogy and particle size distribution of basalt dust wastes. *Science of the Total Environment*, *539*, 560–565. https://doi.org/10.1016/j.scitotenv.2015.08.141

Allen, C. D., Macalady, A. K., Chenchouni, H., Bachelet, D., McDowell, N., Vennetier, M., et al. (2010). A global overview of drought and heat-induced tree mortality reveals emerging climate change risks for forests. *Forest Ecology and Management*, *259*(4), 660–684. https://doi.org/10.1016/J.FORECO.2009.09.001

Almagro, A., Oliveira, P. T. S., Nearing, M. A., & Hagemann, S. (2017). Projected climate change impacts in rainfall erosivity over Brazil. *Scientific Reports*, *7*(1), 8130. https://doi.org/10.1038/s41598-017-08298-y

Archer, D., Kheshgi, H., & Maier-Reimer, E. (1997). Multiple timescales for neutralization of fossil fuel CO_2. *Geophysical Research Letters*, *24*(4), 405–408. https://doi.org/10.1029/97GL00168

Baek, S. H., & Lora, J. M. (2021). Counterbalancing influences of aerosols and greenhouse gases on atmospheric rivers. *Nature Climate Change*, *11*, 958–965. https://doi.org/10.1038/s41558-021-01166-8

Baldwin, J. W., Dessy, J. B., Vecchi, G. A., & Oppenheimer, M. (2019). Temporally compound heat wave events and global warming: An emerging hazard. *Earth's Future*, *7*(4), 411–427. https://doi.org/10.1029/2018EF000989

Beerling, D. J., Kantzas, E. P., Lomas, M. R., Wade, P., Eufrasio, R. M., Renforth, P., et al. (2020). Potential for large-scale CO_2 removal via enhanced rock weathering with croplands. *Nature*, *583*(7815), 242–248. https://doi.org/10.1038/s41586-020-2448-9

Beerling, D. J., Leake, J. R., Long, S. P., Scholes, J. D., Ton, J., Nelson, P. N., et al. (2018). Farming with crops and rocks to address global climate, food and soil security. *Nature Plants*, *4*(3), 138–147. https://doi.org/10.1038/s41477-018-0108-y

Buckingham, F., Henderson, G. M., Holdship, P., & Renforth, P. (2022). Soil core study indicates limited CO_2 removal by enhanced weathering in dry croplands in the UK. *Applied Geochemistry*, *147*, 105482. https://doi.org/10.1016/j.apgeochem.2022.105482

Bullock, L. A., James, R. H., Matter, J., Renforth, P., & Teagle, D. A. H. (2021). Global carbon dioxide removal potential of waste materials from metal and diamond mining. *Frontiers in Climate*, *3*, 694175. https://doi.org/10.3389/fclim.2021.694175

Burrell, A. L., Evans, J. P., & De Kauwe, M. G. (2020). Anthropogenic climate change has driven over 5 million km^2 of drylands towards desertification. *Nature Communications*, *11*(1), 3853. https://doi.org/10.1038/s41467-020-17710-7

Calabrese, S., Wild, B., Bertagni, M. B., Bourg, I. C., White, C., Aburto, F., et al. (2022). Nano- to global-scale uncertainties in terrestrial enhanced weathering. *Environmental Science & Technology*, *56*(22), 15261–15272. https://doi.org/10.1021/acs.est.2c03163

Campbell, J. S., Foteinis, S., Furey, V., Hawrot, O., Pike, D., Aeschlimann, S., et al. (2022). Geochemical negative emissions technologies: Part I. Review. *Frontiers in Climate*, *4*, 879133. https://doi.org/10.3389/fclim.2022.879133

Chen, S., Huang, Y., Zou, J., Shen, Q., Hu, Z., Qin, Y., et al. (2010). Modeling interannual variability of global soil respiration from climate and soil properties. *Agricultural and Forest Meteorology*, *150*(4), 590–605. https://doi.org/10.1016/j.agrformet.2010.02.004

Cook, B. I., Smerdon, J. E., Seager, R., & Coats, S. (2014). Global warming and 21st century drying. *Climate Dynamics*, *43*(9–10), 2607–2627. https://doi.org/10.1007/s00382-014-2075-y

Crowther, T., Todd-Brown, K., Rowe, C., Wieder, W. R., Carey, J. C., Machmuller, M. B., et al. (2016). Quantifying global soil carbon losses in response to warming. *Nature*, *540*(7631), 104–108. https://doi.org/10.1038/nature20150

Davidson, E., & Janssens, I. (2006). Temperature sensitivity of soil carbon decomposition and feedbacks to climate change. *Nature*, *440*(7081), 165–173. https://doi.org/10.1038/nature04514

Fawzy, S., Osman, A. I., Doran, J., & Rooney, D. W. (2020). Strategies for mitigation of climate change: A review. *Environmental Chemistry Letters*, *18*(6), 2069–2094. https://doi.org/10.1007/s10311-020-01059-w

Fuss, S., Canadell, J., Peters, G., Tavoni, M., Andrew, R. M., Ciais, P., et al. (2014). Betting on negative emissions. *Nature Climate Change*, *4*(10), 850–853. https://doi.org/10.1038/nclimate2392

Fuss, S., Lamb, W. F., Callaghan, M. W., Hilaire, J., Creutzig, F., Amann, T., et al. (2018). Negative emissions—Part 2: Costs, potentials and side effects. *Environmental Research Letters*, *13*(6), 063002. https://doi.org/10.1088/1748-9326/aabf9f

Galinato, S. P., Yoder, J. K., & Granatstein, D. (2011). The economic value of biochar in crop production and carbon sequestration. *Energy Policy*, *39*(10), 6344–6350. https://doi.org/10.1016/j.enpol.2011.07.035

Goll, D. S., Ciais, P., Amann, T., Buermann, W., Chang, J., Eker, S., et al. (2021). Potential CO_2 removal from enhanced weathering by ecosystem responses to powdered rock. *Nature Geoscience*, *14*(8), 545–549. https://doi.org/10.1038/s41561-021-00798-x

Gonzalez, P., Neilson, R. P., Lenihan, J. M., & Drapek, R. J. (2010). Global patterns in the vulnerability of ecosystems to vegetation shifts due to climate change. *Global Ecology and Biogeography*, *19*(6), 755–768. https://doi.org/10.1111/j.1466-8238.2010.00558.x

Hartmann, J., & Moosdorf, N. (2012). The new global lithological map database GLiM: A representation of rock properties at the Earth surface. *Geochemistry, Geophysics, Geosystems*, *13*(12), Q12004. https://doi.org/10.1029/2012GC004370

Hengl, T., Mendes de Jesus, J., Heuvelink, G. B. M., Ruiperez Gonzalez, M., Kilibarda, M., Blagotić, A., et al. (2017). SoilGrids250m: Global gridded soil information based on machine learning. *PLoS One*, *12*(2), e0169748. https://doi.org/10.1371/journal.pone.0169748

IPCC. (2018). In V. Masson-Delmotte, P. Zhai, H.-O. Pörtner, D. Roberts, J. Skea, et al. (Eds.), *Global warming of 1.5°C*. An IPCC Special Report on the impacts of global warming of 1.5°C above pre-industrial levels and related global greenhouse gas emission pathways, in the context of strengthening the global response to the threat of climate change, sustainable development, and efforts to eradicate poverty.

IPCC. (2022). In H.-O. Pörtner, D. C. Roberts, M. Tignor, E. S. Poloczanska, K. Mintenbeck, et al. (Eds.), *Climate change 2022: Impacts, adaptation and vulnerability. Contribution of Working Group II to the sixth assessment report of the Intergovernmental Panel on Climate Change* (p. 3056). Cambridge University Press. https://doi.org/10.1017/9781009325844

Jeswani, H. K., Saharudin, D. M., & Azapagic, A. (2022). Environmental sustainability of negative emissions technologies: A review. *Sustainable Production and Consumption*, *33*, 608–635. https://doi.org/10.1016/j.spc.2022.06.028

Kantzas, E. P., Val Martin, M., Lomas, M. R., Eufrasio, R. M., Renforth, P., Lewis, A. L., et al. (2022). Substantial carbon drawdown potential from enhanced rock weathering in the United Kingdom. *Nature Geoscience*, *15*(5), 382–389. https://doi.org/10.1038/s41561-022-00925-2

Kanzaki, Y. (2022). Lithos-erw/SCEPTER: Submission to GMDD (v0.9) [Code]. *Zenodo*. https://doi.org/10.5281/zenodo.5835413

Kanzaki, Y., Planavsky, N. J., & Reinhard, C. T. (2023). New estimates of the storage permanence and ocean co-benefits of enhanced rock weathering. *PNAS Nexus*, *2*(4), pgad059. https://doi.org/10.1093/pnasnexus/pgad059

Kanzaki, Y., Zhang, S., Planavsky, N. J., & Reinhard, C. T. (2022). Soil cycles of elements simulator for predicting TERrestrial regulation of greenhouse gases: SCEPTER v0.9. *Geoscientific Model Development*, *15*(12), 4959–4990. https://doi.org/10.5194/gmd-15-4959-2022

Kay, J. E., Deser, C., Phillips, A., Mai, A., Hannay, C., Strand, G., et al. (2015). The Community Earth System Model (CESM) Large Ensemble Project: A community resource for studying climate change in the presence of internal climate variability. *Bulletin of the American Meteorological Society*, *96*(8), 1333–1349. https://doi.org/10.1175/BAMS-D-13-00255.1

Larsen, I. J., Montgomery, D. R., & Greenberg, H. M. (2014). The contribution of mountains to global denudation. *Geology*, *42*(6), 527–530. https://doi.org/10.1130/G35136.1

Lindner, M., Maroschek, M., Netherer, S., Kremer, A., Barbati, A., Garcia-Gonzalo, J., et al. (2010). Climate change impacts, adaptive capacity, and vulnerability of European forest ecosystems. *Forest Ecology and Management*, *259*(4), 698–709. https://doi.org/10.1016/J.FORECO.2009.09.023

Lukin, V. V., & Epplin, F. M. (2003). Optimal frequency and quantity of agricultural lime applications. *Agricultural Systems*, *76*(3), 949–967. https://doi.org/10.1016/S0308-521X(02)00016-1

Mengel, M., Levermann, A., Frieler, K., Robinson, A., Marzeion, B., & Winkelmann, R. (2016). Future sea level rise constrained by observations and long-term commitment. *Proceedings of the National Academy of Sciences*, *113*(10), 2597–2602. https://doi.org/10.1073/PNAS.1500515113

Midgley, G., & Bond, W. (2015). Future of African terrestrial biodiversity and ecosystems under anthropogenic climate change. *Nature Climate Change*, *5*(9), 823–829. https://doi.org/10.1038/nclimate2753

Minx, J. C., Lamb, W. F., Callaghan, M. W., Fuss, S., Hilaire, J., Creutzig, F., et al. (2018). Negative emissions—Part 1: Research landscape and synthesis. *Environmental Research Letters*, *13*(6), 063001. https://doi.org/10.1088/1748-9326/aabf9b

Navarre-Sitchler, A. K., & Brantley, S. L. (2007). Basalt weathering across scales. *Earth and Planetary Science Letters*, *261*(1–2), 321–334. https://doi.org/10.1016/j.epsl.2007.07.010

NOAA National Centers for Environmental Information. (2021). State of the climate: Global climate report for annual 2020. Published online January 2021. Retrieved from https://www.ncdc.noaa.gov/sotc/global/202013

Nottingham, A. T., Whitaker, J., Ostle, N. J., Bardgett, R. D., McNamara, N. P., Fierer, N., et al. (2019). Microbial responses to warming enhance soil carbon loss following translocation across a tropical forest elevation gradient. *Ecology Letters*, *22*(11), 1889–1899. https://doi.org/10.1111/ele.13379

Otto-Bliesner, B. L., Brady, E. C., Fasullo, J., Jahn, A., Landrum, L., Stevenson, S., et al. (2016). Climate variability and change since 850 CE: An ensemble approach with the Community Earth System Model. *Bulletin of the American Meteorological Society*, *97*(5), 735–754. https://doi.org/10.1175/BAMS-D-14-00233.1

Payne, A. E., Demory, M. E., Leung, L. R., Ramos, A. M., Shields, C. A., Rutz, J. J., et al. (2020). Responses and impacts of atmospheric rivers to climate change. *Nature Reviews Earth & Environment*, *1*(3), 143–157. https://doi.org/10.1038/s43017-020-0030-5

Rahmstorf, S. (2007). A semi-empirical approach to projecting future sea-level rise. *Science*, *315*(5810), 368–370. https://doi.org/10.1126/science.1135456

Ridgwell, A., & Hargreaves, J. C. (2007). Regulation of atmospheric CO_2 by deep-sea sediments in an Earth system model. *Global Biogeochemical Cycles*, *21*(2), GB2008. https://doi.org/10.1029/2006GB002764

Strefler, J., Amann, T., Bauer, N., Kriegler, E., & Hartmann, J. (2018). Potential and costs of carbon dioxide removal by enhanced weathering of rocks. *Environmental Research Letters*, *13*(3), 034010. https://doi.org/10.1088/1748-9326/aaa9c4

Taylor, L. L., Quirk, J., Thorley, R., Kharecha, P. A., Hansen, J., Ridgwell, A., et al. (2016). Enhanced weathering strategies for stabilizing climate and averting ocean acidification. *Nature Climate Change*, *6*(4), 402–406. https://doi.org/10.1038/nclimate2882

Tuanmu, M.-N., & Jetz, W. (2014). A global 1-km consensus land-cover product for biodiversity and ecosystem modelling. *Global Ecology and Biogeography*, *23*(9), 1031–1045. https://doi.org/10.1111/geb.12182

Wang, X., Piao, S., Ciais, P., Janssens, I. A., Reichstein, M., Peng, S., & Wang, T. (2010). Are ecological gradients in seasonal Q_{10} of soil respiration explained by climate or by vegetation seasonality? *Soil Biology and Biochemistry*, *42*(10), 1728–1734. https://doi.org/10.1016/j.soilbio.2010.06.008

West, L. J., Banwart, S. A., Martin, M. V., Kantzas, E., & Beerling, D. J. (2023). Making mistakes in estimating the CO_2 sequestration potential of UK croplands with enhanced weathering. *Applied Geochemistry*, *151*, 105591. https://doi.org/10.1016/j.apgeochem.2023.105591

West, T. O., & McBride, A. C. (2005). The contribution of agricultural lime to carbon dioxide emissions in the United States: Dissolution, transport, and net emissions. *Agriculture, Ecosystems & Environment*, *108*(2), 145–154. https://doi.org/10.1016/j.agee.2005.01.002

Williams, A. P., Cook, E. R., Smerdon, J. E., Cook, B. I., Abatzoglou, J. T., Bolles, K., et al. (2020). Large contribution from anthropogenic warming to an emerging North American megadrought. *Science*, *368*(6488), 314–318. https://doi.org/10.1126/science.aaz9600

World Meteorological Organization. (2020). State of the global climate 2020. ISBN 978-92-63-11264-4.

Zhang, M., Liu, N., Harper, R., Li, Q., Liu, K., Wei, X., et al. (2017). A global review on hydrological responses to forest change across multiple spatial scales: Importance of scale, climate, forest type and hydrological regime. *Journal of Hydrology*, *546*, 44–59. https://doi.org/10.1016/J.JHYDROL.2016.12.040

Zhao, F., Wu, Y., Hui, J., Sivakumar, B., Meng, X., & Liu, S. (2021). Projected soil organic carbon loss in response to climate warming and soil water content in a loess watershed. *Carbon Balance and Management*, *16*(1), 24. https://doi.org/10.1186/s13021-021-00187-2